Appl. Phys. A (2015) 121:261–271
DOI 10.1007/s00339-015-9429-0

Applied Physics A
Materials Science & Processing

Synthesis of rattle-type Ag@Al_2O_3 nanostructure by laser-induced heating of Ag and Al nanoparticles

Rina Singh[1,2] · **R. K. Soni**[1]

Received: 16 May 2015 / Accepted: 10 August 2015 / Published online: 20 August 2015

Abstract A simple and flexible method has been presented for the fabrication of rattle-type Ag@Al_2O_3 nanostructures in water and polyvinyl pyrrolidone polymer solution based on laser-induced heating of mixture of silver (Ag) and aluminium (Al) nanoparticles by 532-nm laser. Silver and aluminium nanoparticles were prepared by pulsed laser ablation in liquid using same laser wavelength. The transmission electron micrographs revealed morphological changes from sintered-/intermediate-type structure in water medium and jointed structure (heterostructures) in polymer solution to rattle-type structure with changing irradiation time. At longer irradiation time, the Kirkendall effect becomes dominant due to diffusion rate mismatch between the two metals at the interface and facilitates the formation of porous alumina shell over silver core. The morphology and chemical composition of the nanostructures were characterized by transmission electron micrograph, high-resolution transmission electron micrograph and energy-dispersive X-ray analysis. The melting response of alumina (Al_2O_3), aluminium and silver nanoparticles with 532-nm laser wavelength provides novel pathway for rattle-type formation.

Graphical Abstract

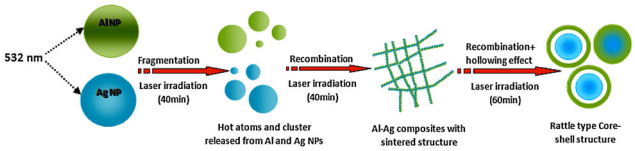

1 Introduction

Bimetallic nanoparticles (NPs) in a form of core–shell, alloy and rattle-type nanostructure exhibit diverse properties, which could be explored for variety of applications such as efficient selective catalysts, drug delivery, sensors, SERS-based molecular probe, environmental remediation and filters [1–4]. The core–shell structure enhances the interaction between the metal core and the shell, thus creating more active boundary sites [5]. Because of this, one may incorporate additional functional groups or organometallic catalysts inside the shells. The core–shell NPs are considered as an efficient way to inhibit agglomeration or oxidation of the metal NPs. The morphology of nanostructures has a significant influence on their properties. Therefore, the controllable synthesis of nanostructures morphology is highly anticipated. In spite of tremendous progress in the synthesis of core–shell NPs, there is still no general method for control and reliable synthesis of bimetallic core–shell NPs using laser-induced heating methodology.

Recently, a special class of core–shell NPs with core in a hollow shell, called rattle-type structures or yolk–shell structures, has drawn much attention because of their distinct structural properties and diverse functionalities of shells for potential applications in catalysis and nanomedicine [6–10]. It possesses spherical porous shells and solid

✉ Rina Singh
rina_it@rediffmail.com; rinasingh.crri@nic.in

[1] Physics Department, Indian Institute of Technology Delhi, New Delhi 110016, India

[2] Present Address: Environment Science Division, CSIR-Central Road Research Institute, New Delhi 110065, India

cores with a variable space or void between them. Because of their unique structure, they exhibit enhanced surface area and high stability. The shells protect the core element from the outside environment and thus maintain its compositional and structural integrity and prevent its aggregation or sintering into large particles [11, 12].

Porous micro- and nanostructured materials with tailored morphologies and tunable pore sizes have great potential for applications in environmental remediation like wastewater treatment, gas sensors, absorbent and catalysis [6, 7]. The major methods to prepare rattle-type structures are hard-/soft-templating methods, Kirkendall, Ostwald ripening effect and selective etching [8–10, 13–15]. In a spherical material system, when the fast diffusion species is enclosed by the slower one, the Kirkendall effect transforms the system by forming hollow structures of a compound shell [16]. The void space in hollow particles or rattle structures has been used for refractive index modulation, density reduction and enhancement of active area for catalysis [17]. Their open hollow structure enables both the outer and inner surfaces of the catalyst to come into contact with the reactants giving enhanced catalytic performances [18, 19]. Various types of rattle nanostructures like metal NPs@polymer, metal NPs@oxides, metal–metal bimetal NPs@oxides/polymers have been synthesized; however, these methods are often complicated because of tedious procedures and poor reproducibility. Thus, there is a need to develop simple, controllable and environmental friendly method for the synthesis of the rattle-type nanostructures.

A very simple, versatile and one-step method called pulsed laser ablation in liquid (PLAL) has been developed to synthesize variety of emerging materials [20–23]. Earlier studies using PLAL mainly focused on the preparation of noble NPs via laser ablation of metal targets and the modification of the NP size and shape. However, in the last 5 years, in addition to the conventional synthesis of metal NPs, researchers have started to adequately use the unique features of PLAL to fabricate various nanostructures with novel morphologies (core–shell, trimetallic nanocomposites (NCs), alloys and polyoxometalates), microstructures and phases, which makes it possible to explore novel properties and applications for the new products [23–26]. The PLAL offers many advantages over chemical synthesis strategies; for example, laser-synthesized metal nanoparticles are charged, and hence, stable, toxic chemical precursors like surfactants are not required, and thus, the colloids are ultrapure, and the method can be applied universally to almost any material and solvents [21]. Al NPs could be useful in the long run due to the abundance of the Al element and its relatively lower costs compared to other elements like Ag and Au. In addition, as a plasmonic material, Al outperforms noble metals in terms of range of plasmonic active wavelengths and near-field enhancement [27]. Combining Al with Ag or Au, an efficient catalyst could be designed. Silver supported on alumina (Al_2O_3) has been reported to be active and stable catalyst for selective catalytic reduction of nitrogen oxides with various hydrocarbons [28, 29]. Alumina because of its large porosity and high surface area helps in proper dispersion of silver NPs and gold NPs on its surface and facilitates the formation of novel composite catalysts with a high density of active sites [30–32]. Various porous shells have been prepared to encapsulate metal NPs, isolating the active cores and providing convenient channels for reactant species to reach the surface of the active cores [11]. However, to the best of our knowledge, the one-pot synthesis of $Ag@Al_2O_3$ using laser-induced heating has rarely been reported. Here, we present a simple two-step strategy for the fabrication of rattle-type $Ag–Al_2O_3$ core–shell structures in water and polymer solution using PLAL and post-laser irradiation (PLI).

2 Experimental

Silver and aluminium NPs were prepared by ablating sliver and aluminium metal plates (99.99 % pure) for 20 min in deionized water and polyvinyl pyrrolidone (PVP) polymer using second-harmonics (532 nm) wavelength of Nd: YAG laser (Quanta Systems, Model SYL 202) having 5-ns pulse duration and 10-Hz pulse repetition rate. The laser beam was focused by a convex lens of focal length 150 mm to obtain a laser spot size of 0.5 mm on the target immersed in liquid. The laser fluence used for silver and aluminium ablation was 14.3 and 4.5 J/cm^2, respectively; the lower fluence for aluminium ablation was necessary because of the lower melting point of aluminium compared to silver; further aluminium oxidizes rapidly at higher laser fluence. The metal plate (Ag or Al) was placed at the bottom of a glass vessel filled with 5 ml of deionized water or 0.001 mM concentration of aqueous solution of PVP (24 kDa, Central Drug House). The freshly prepared nanoparticle solutions were then mixed in 1:1 volumetric ratios to obtain 3 ml as-mixed Ag–Al solution. The as-mixed solution was post-irradiated with an unfocussed beam of the same laser at fluence 0.6 J/cm^2 for different time. The irradiated nanoparticle solutions were immediately characterized by UV–Vis absorption spectroscopy using a dual-beam spectrophotometer (PerkinElmer Lambda35) having spectral resolution of 0.5 nm. The extinction spectra of the samples were periodically monitored at regular intervals for their chemical stability and nanoparticle aggregation. TEM analysis was performed at 100 kV with a Philips Model CM 12 Microscope. HRTEM analysis was performed at an accelerating voltage of

200 kV with Technai G20-stwin HRTEM microscope. The HRTEM was equipped with energy-dispersive X-ray analysis (EDX) for elemental studies. For TEM and HRTEM, the nanoparticle suspensions were dropped onto a carbon-coated Cu grid and then dried at room temperature.

3 Results and discussion

3.1 Synthesis and structural characterization

Figure 1 shows the TEM image of morphological evolution of Ag–Al nanocomposites (NCs) in deionized water with changing post-irradiation time. Initially, sintered-type structure is observed for 40 min of post-irradiation, as shown in Fig. 1a. Due to laser-induced electric dipole moment, the NPs tend to align one dimensionally to minimize electrostatic potential of the dipole–dipole interaction leading to network-type structure [33]. After further irradiation for 20 min, gradual morphological transformation to stable nearly spherical rattle-type core–shell structure is seen due to enhanced materials diffusion and interaction at the core–shell interface. The TEM analysis reveals narrow size dispersion and isolated particles of mean size 25 nm with shell thickness of 4–6 nm. Further, the aluminium shell gets highly oxidized in water forming porous γ-alumina along with a hollow region or variable gap between the core and shell, similar to the rattle-type structure formed in other synthesis strategies [30–34]. The high-temperature and high-pressure dynamics in PLAL resulted in the formation of crystalline γ-alumina.

Along with spherical rattle particles, the TEM image also reveals shape anisotropy in the form of dumbbell or ellipsoidal-type structure as shown in Fig. 2 (inset shows dumbbell structure). Such structures could be formed due to anisotropic local heating of the silver core during laser heating in deionized water. The anisotropic growth in a colloidal NPs results because of two different mechanisms: oriented attachment and Ostwald ripening [35]. The oriented attachment growth mechanism occurs through self-assembly or attachment and coalescence of NPs at their energetically favourable crystal planes [35]. The driving force for such mechanism is the reduction of surface energy after the smoothening of their interfaces. However, in Ostwald ripening growth mechanism, the dissolution of smaller NPs in the solution because of their large surface energy to form large particles of high-energy crystal planes leads to oriented growth along these faces.

Figure 3a–c shows the HRTEM, SAED and EDX pattern, respectively, of Ag–Al_2O_3 rattle-type particles in deionized water. Alumina being a dielectric material and on the basis of scattering effect, it is possible to differentiate the two, since the metallic silver because of large electron density will scatter more and therefore will appear dark as compared to alumina (clearly seen in both TEM and HRTEM images). SAED pattern (Fig. 3b) shows *d* spacing corresponding to both γ-alumina and silver phase. The *d* spacing value of 0.23, 0.20 and 0.88 nm corresponds to (222), (400) and (840) planes of γ-alumina, and the *d* values of 0.12, 0.10 and 0.83 nm correspond to (311), (400) and (422) planes of silver phase. The high-resolution image reveals lattice fringe separation of 0.779 nm corresponding to γ-phase of alumina [31]. Earlier reports on pulsed laser ablation of aluminium in water have also confirmed the formation of γ-Al_2O_3 [36, 37]. The EDX spectrum shows the presence of aluminium, oxygen and silver besides copper arising from the carbon-coated grid. The large peak intensity of aluminium and oxygen

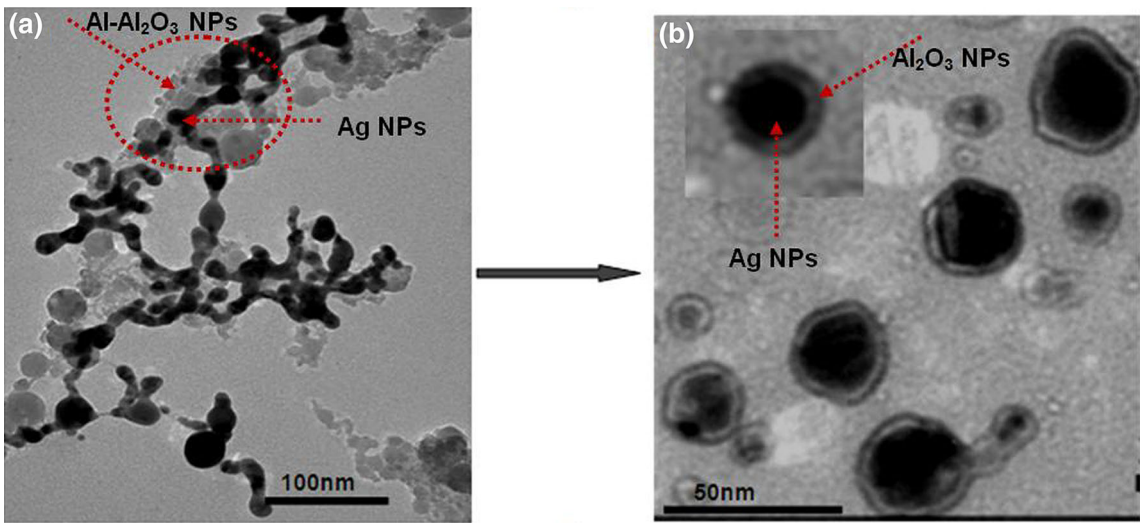

Fig. 1 TEM images of Ag–Al nanocomposite post-irradiated with 532-nm laser in deionized water for **a** 40 min and **b** 60 min. *Inset* in (**b**) shows complete core–shell structure with Ag (*dark*) as core and Al_2O_3 (*grey colour*) as shell

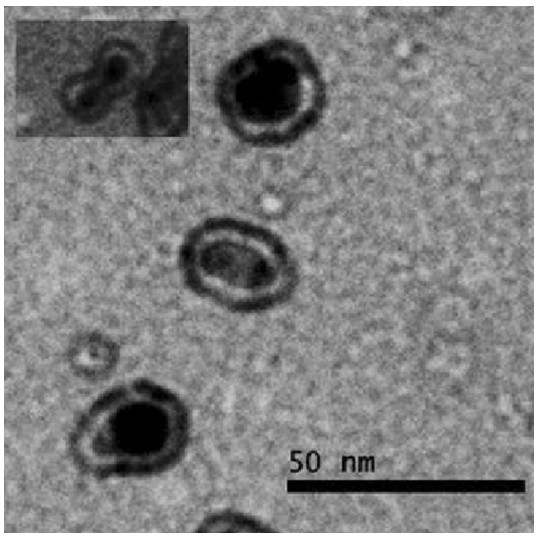

Fig. 2 TEM image of Ag–Al_2O_3 rattle-type nanoparticles post-irradiated for 60 min in deionized water. The image shows non-spherical rattle particles, and *inset* shows rattle-type dumbbell structure

compared to silver in the spectrum corroborates the formation of aluminium oxide on the surface of the rattle particles encapsulating the silver core.

Figure 4 shows the TEM image of 1:1 ratio of Ag–Al in 0.001 mM PVP solution at different post-irradiation time. Post-irradiation of 40 min in PVP solution reveals weakly aggregated Al–Al_2O_3 as well as dispersed small spherical silver particles in the TEM image. The morphology of the NC shows strong dependence on concentration of the polymer used and the particle characteristics [38, 39]. Figure 4a shows distinguishable Ag nanoparticles (dark) adsorbed on Al/Al_2O_3 aggregates (grey) [40].

Figure 5a–c show the HRTEM, SAED and EDX pattern, respectively, of Ag–Al_2O_3 rattle-type particles in 0.001 mM PVP solution. The HRTEM image shows both dark and bright contrast, suggesting the formation of composite structure. The measured lattice spacing of 0.28 nm in HRTEM image corresponds to (220) plane of γ-Al_2O_3 oxide. The selected-area electron diffraction (SAED) pattern of Al–Ag NCs exhibits ring patterns; the diffraction spots are assigned to (222), (400), (440), (444), (800) and (840) planes of γ-Al_2O_3 crystals (JCPDS#10-0425) and confirm polycrystalline nature of Al_2O_3. The EDX spectrum shows the presence of aluminium, oxygen and silver in the Ag–Al_2O_3 rattle-type particles.

3.2 Formation mechanism

Scheme 1 illustrates laser-assisted formation of rattle-type Ag–Al_2O_3 core–shell particles in water. An equal volume of Al and Ag colloidal solutions, prepared by PLAL, are mixed and subjected to PLI for different times to initially form core–shell structures followed by sintered-/intermediate-type structure and finally rattle-type structures (elucidated with experimental TEM pictures observed at different post-irradiation time). In the physical mixture of Ag and Al colloidal NPs, absorption for Ag NPs is larger than Al NPs at 532-nm wavelength [41, 42]. However, the dielectric alumina at the surface of aluminium melts faster than the aluminium or silver metal. The TEM morphology in Fig. 1a, b clearly shows the presence of melted form of alumina (light grey colour) and silver particles (black). Rothenberg et al. worked on the laser-produced plasma (LPP) behaviour of metal (Al) and dielectric (Al_2O_3) under the influence of intense laser beam [43]. Their results showed that the threshold fluence for LPP formation in dielectric was much lower than for pure metal. This unexpected result was analysed taking into account the differences in the absorptivity, thermal diffusivity and volatility of the two materials [43, 44]. In our case, the melting response of Al_2O_3, Al and Ag NPs provides novel pathway for NC formation. For the formation of LPP from a solid target, a minimum value of absorbed energy density (U_e) at the surface is required. The threshold value U_{eth} is lower for more volatile materials with smaller heat capacity, but is more difficult to reach in materials with higher thermal diffusivity which results in higher U_{eth} value,

$$U_e = F\,(1 - R_{ref})\,\alpha_{abs}, \tag{1}$$

where F is the incident fluence, R_{ref} is the reflectivity of material and α_{abs} is the absorption coefficient. The U_{eth} value in Al is lower than that in alumina due to its higher volatility; however, at the laser fluence sufficient for LPP in alumina, LPP in Al would not be obtained because of its greater thermal diffusivity which would not allow U_e to attain U_{eth}. Such effects in alumina could lead to a significant enhancement in the vaporization of surface atoms and thus explains the melting of alumina for the formation of rattle-type NCs [44, 45].

At longer irradiation time, the Kirkendall effect becomes dominate, due to diffusion rate mismatch between the two metals at the interface, which results in the formation of hollow region between the silver core and Al_2O_3 shell. Growth of nanoparticles from a solid target immersed in liquid by nanosecond laser ablation involves complex high-temperature high-pressure plasma generation and rapid quenching in surrounding dense medium. The secondary ablation or pulsed laser heating of metal NPs is often used for size and shape modifications of nanoparticles in liquid [44, 45]. In PLI of the laser-generated particles, free electron excitation and rapid energy transfer to lattice, in picosecond time scale, produce excessive heat which transforms the solid metal into a molten phase. The reaction of molten material with vapours arising from the

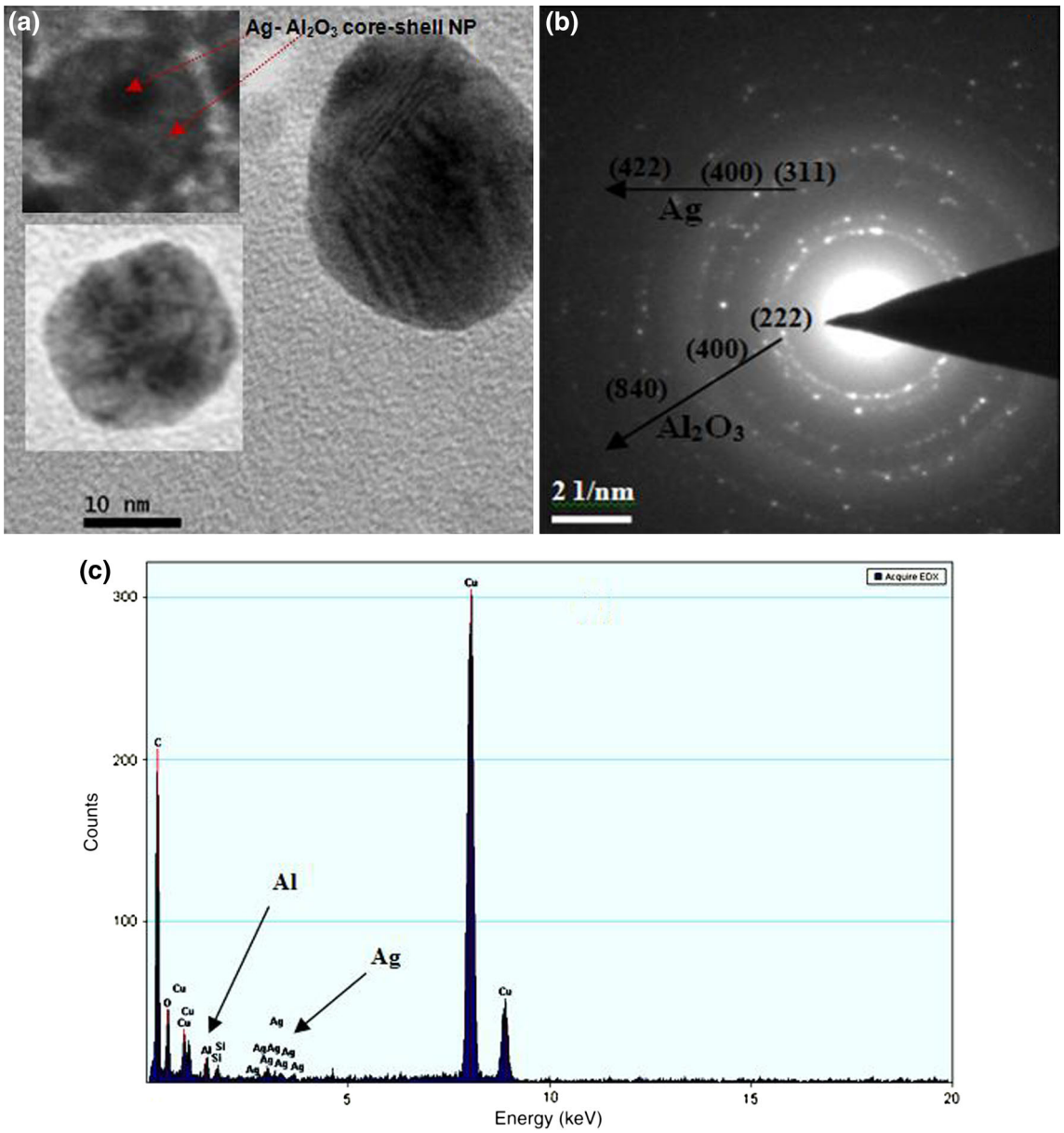

Fig. 3 **a** HRTEM image of Al–Ag NCs in deionized water subjected to post-ablation nanosecond pulsed laser heating for 60 min. *Inset* image shows complete core–shell morphology, **b** selected-area electron diffraction pattern of Ag–Al NCs subjected to post-ablation nanosecond pulsed laser heating for 60 min, the *d* spacing value of 0.23, 0.20 and 0.88 nm corresponds to (222), (400) and (840) planes of γ alumina, and the *d* values of 0.12, 0.10 and 0.83 nm correspond to (311), (400) and (422) planes of Ag phase, **c** EDX of Al–Ag in water showing Al and Ag as main constituent elements

surrounding liquid or other nanoparticles in the solution can alter the final product size. In addition, laser–nanoparticle interaction can simultaneously cause photofragmentation of large particles and photofusion and sintering of small particles [46]. The formation of nanocomposite requires physical interaction of the nanoparticles when one of them is in the molten phase. Such a condition prevails only during the laser pulse, in our case nanosecond, as the particles solidify rapidly via heat dissipation to surrounding liquid.

Relatively small lattice mismatch of Ag (4.0853 Å) and Al (4.0495 Å) and similar FCC crystal structure makes it possible to grow aluminium layer over the surface of Ag nanoparticle or vice versa without interfacial strain under appropriate conditions [47, 48]. Moreover, the cohesive energy determines the stability and morphology of NCs since the structure with higher cohesive energy tends to be more stable [49, 50]. The experimental cohesive energy of bulk Al (3.39 eV per atom) [49, 51] and Ag (2.95 eV per atom) [50] suggests higher stability for Al than for Ag. The

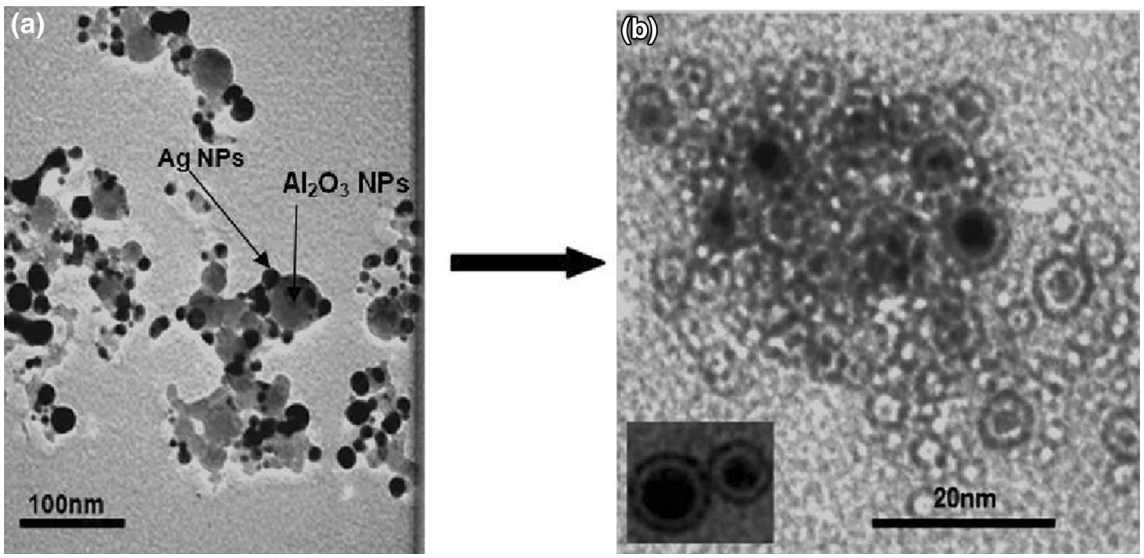

Fig. 4 TEM images of Ag–Al NC post-irradiated with 532-nm laser wavelength in 0.001 mM PVP polymer, **a** 40 min (*grey colour* aluminium oxide is in fused form and over that small silver NPs (*dark colour*) are deposited) **b** 60 min (*inset* showing complete rattle nanostructure)

surface energy of Al–Al_2O_3 is further reduced in comparison with pure Al and Ag; therefore, Ag–Al_2O_3 core–shell particle could be fabricated as a stable structure. In addition, the analysis of diffusion behaviour and atomic distribution suggest that the minimization of surface energy tends to form Al surface segregation because of its lower surface energy and faster diffusivity than silver and gold.

It is now well established that differential solid-state diffusion rates of the two mixing reactants in an alloying or oxidation reaction can produce porous structures [16, 17]. The hollowing occurs through vacancy exchange rather than direct interchange of atoms. The nanoscale pores can develop inside nanocrystals with a mechanism analogous to void formation in Kirkendall effect. In the case of bimetallic Ag–Al NCs, Al–Al_2O_3 occupies surface or shell position due to its lower surface energy compared to silver. Furthermore, the diffusion rate mismatch between Ag and Al creates vacancies in the Al side near the Ag–Al interface which renders aluminium shell porous in the Ag–Al_2O_3 core–shell structure. Within the small volume of the transforming nanocrystal, the supersaturated vacancy will coalesce into a single void [13].

In as-mixed Ag–(Al–Al_2O_3) NPs solution, both Al–Al_2O_3 and Ag NPs can be excited effectively by 532-nm laser, though absorption in Ag NPs is greater than in Al NPs [41, 52]. Nanoparticles prepared in deionized water are mostly in physical contact; therefore, their morphology reveals interconnected structures. As some Al NPs reach their melting point before Ag NPs, due to lower melting point of Al (660 °C) compared to Ag (961 °C), and size-related melting depression, significant laser-induced heating of nanocomposite can be achieved [53–55]. The melting depression for aluminium is more than for silver; therefore, both Ag and Al NPs reach high temperature and subsequently join together to form sintered or chain-type structure as illustrated in Fig. 1a. Finally, post-irradiation for 60 min results in complete melting of the particles, and the lower surface tension and surface energy of Al_2O_3 transform sintered NCs into Ag–Al_2O_3 rattle-type core–shell particles [56, 57]. These NPs have tendency to aggregate in water after few hours of residency and therefore require stabilizer such as PVP polymer to prevent their aggregation.

Scheme 2 illustrates laser-assisted rattle-type core–shell particle formation in PVP solution. Here, initial polymer-coated Al and Ag NPs under the influence of laser heating form an intermediate structure, consisting of small silver particles deposited on pure aluminium surface, which transforms into core–shell structure and finally to the rattle-type structure. The aggregation of NPs after each laser pulse depends on the coverage of NPs surface by stabilizer molecules and on the probability of collision between the two particles like melted Al NPs with photofragments of silver or vice versa [58]. Recent results have demonstrated that photofragmentation of NPs in the presence of strong ligands leads to the formation of fine NPs rather than large sintered structures [38, 41]. Scheme 2 also suggests the formation of fine NPs deposited or supported on alumina surface rather than formation of sintered-type structure in the presence of polymer (Fig. 4a). As silver NPs absorb the 532-nm laser radiation more efficiently than aluminium NPs, the photofragmentation of silver NPs may result in the formation of smaller particles. On the other hand, the melting and fusion of small aluminium particles take place

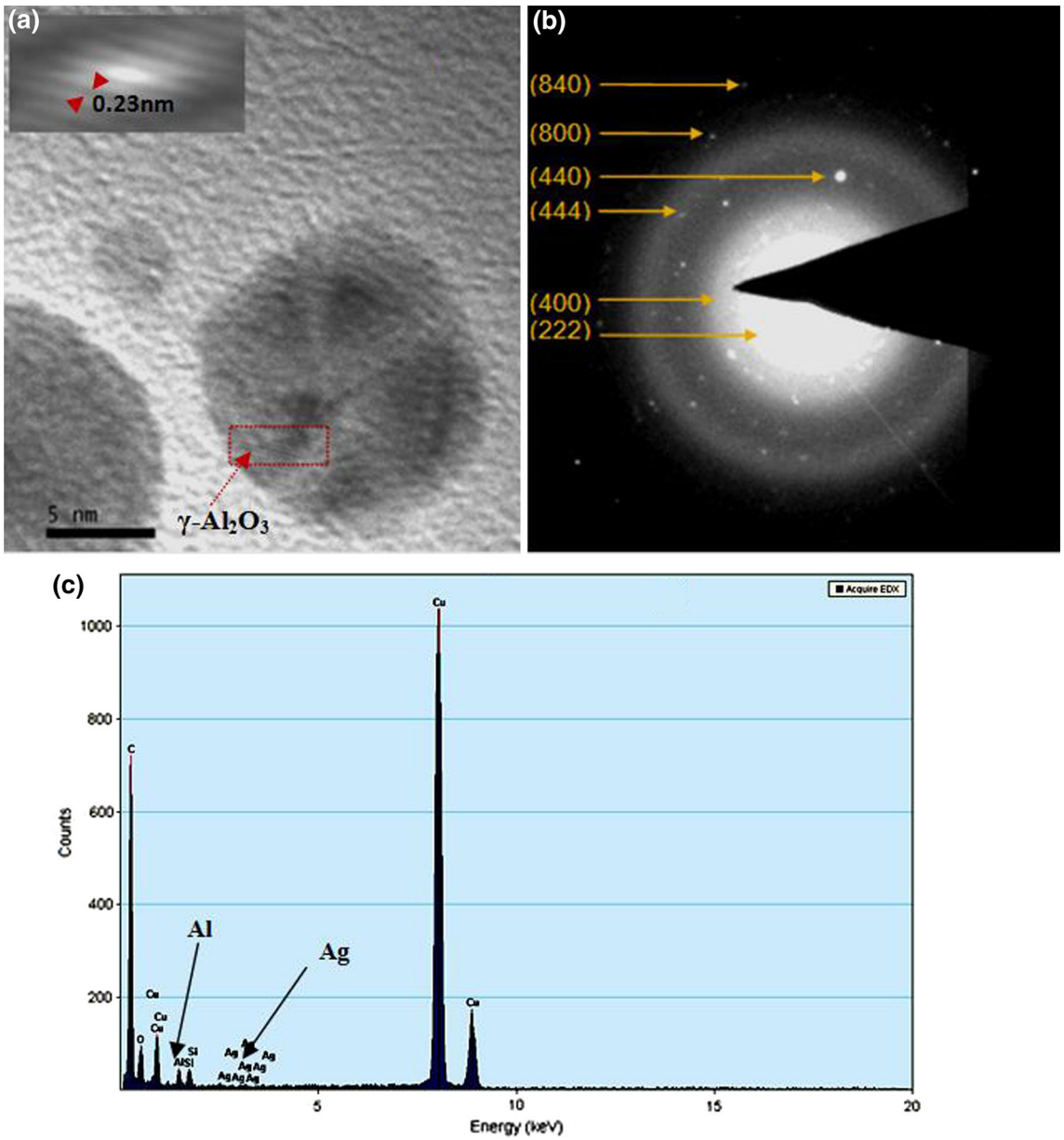

Fig. 5 **a** HRTEM image of Al–Ag NCs in 0.001 mM PVP subjected to post-ablation nanosecond pulsed laser heating for 60 min. *Inset* shows the lattice fringes 0.23 nm corresponding to γ-alumina, **b** selected-area electron diffraction pattern of Ag–Al NCs subjected to post-ablation nanosecond pulsed laser heating for 60 min, **c** EDX of Al–Ag in polymer showing Al and Ag as constituent elements

rapidly than silver particles due to their large melting depression than silver particles; the large agglomerated oxide-coated Al–Al_2O_3 particles shown in Fig. 4a are formed by photofusion of small aluminium particles in the polymer solution. As Al_2O_3 is a porous material with very high surface area, it can support wide dispersion of deposited silver nanoparticles which could be useful for metal-enhanced spectroscopy applications. Longer post-irradiation for 60 min changes the morphology to stable rattle-type structure, Fig. 4b. The laser ablation of aluminium in PVP solution usually produces oxide-free chemically pure Al nanoparticles because of excellent steric stability of the polymer [26, 59]. However, concomitant loss of steric stability and enhancement in oxidation rate at longer post-irradiation time result in Al_2O_3-coated aluminium particles.

In addition to the protecting ligand, the concentration of the parent NPs is also an important factor as it determines the concentration of the photofragments. The lower concentration of parent nanoparticles lowers the released photofragments concentrations and consequently their collision probability. These conditions do not support the formation of sintered structures but suitable for formation of spherical NPs [36, 53]. The spherical morphology in

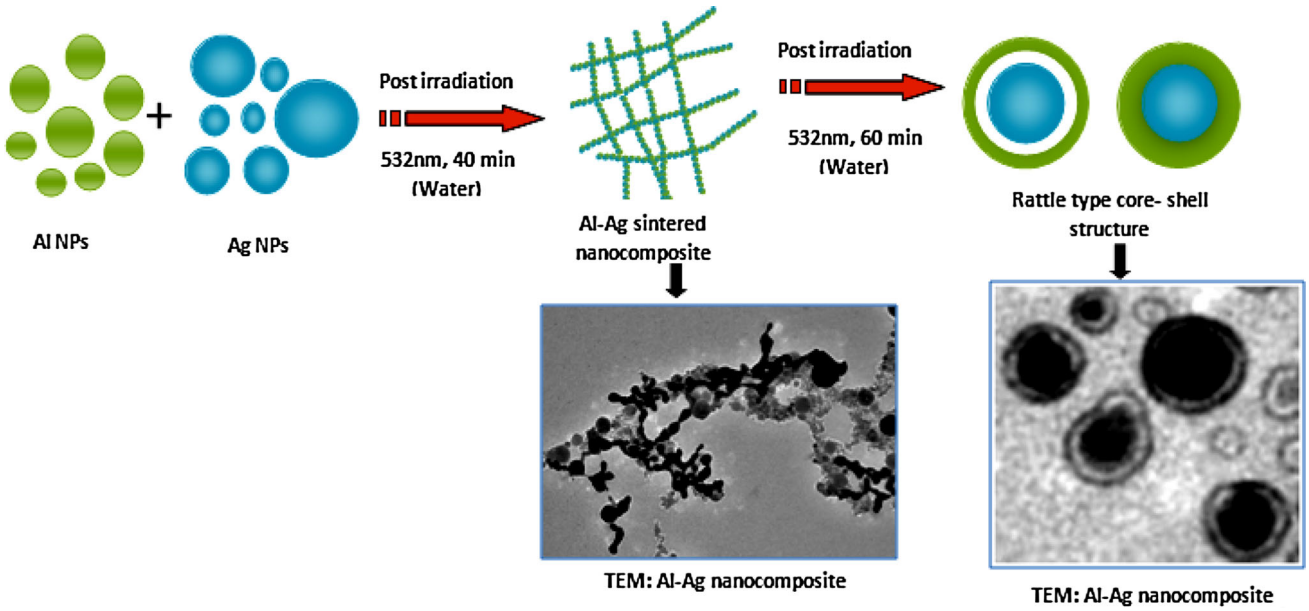

Scheme 1 Illustration of the evolution procedure from sintered structure to core–shell and finally to rattle structure by pulsed laser ablation process

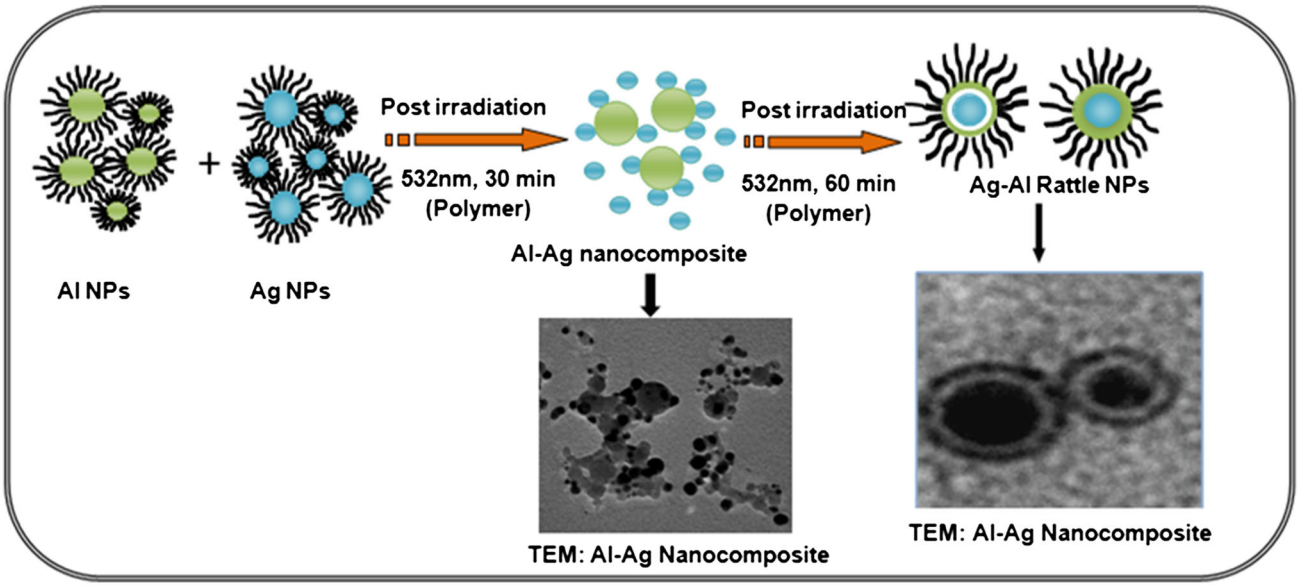

Scheme 2 Illustration of the evolution procedure from sintered structure to core–shell and finally to rattle structure by pulsed laser ablation process in polymer matrix

PVP is mainly due to steric stability provided by the polymer because of its limited diffusion or particle collision for fusion.

3.3 UV–Vis absorption

Figure 6 shows the UV–visible spectra of Al, Ag and as-mixed Ag–Al solution in a 1:1 ratio before and after the laser irradiation in water. In water, aluminium NPs initially show a weak localized surface plasmon resonance (LSPR) absorption band around 225 nm and featureless absorption spectrum in the visible wavelength region (Fig. 6a, curve 1); however, after 2–3 h of residency, a new band with maximum at 264 nm appears. The LSPR peak of pure aluminium NPs has been experimentally observed at 210 nm in ethanol and acetone [60] in agreement with the theoretically calculated peak wavelength in deep UV region 200–220 nm [61, 62]. The large red shift of peak

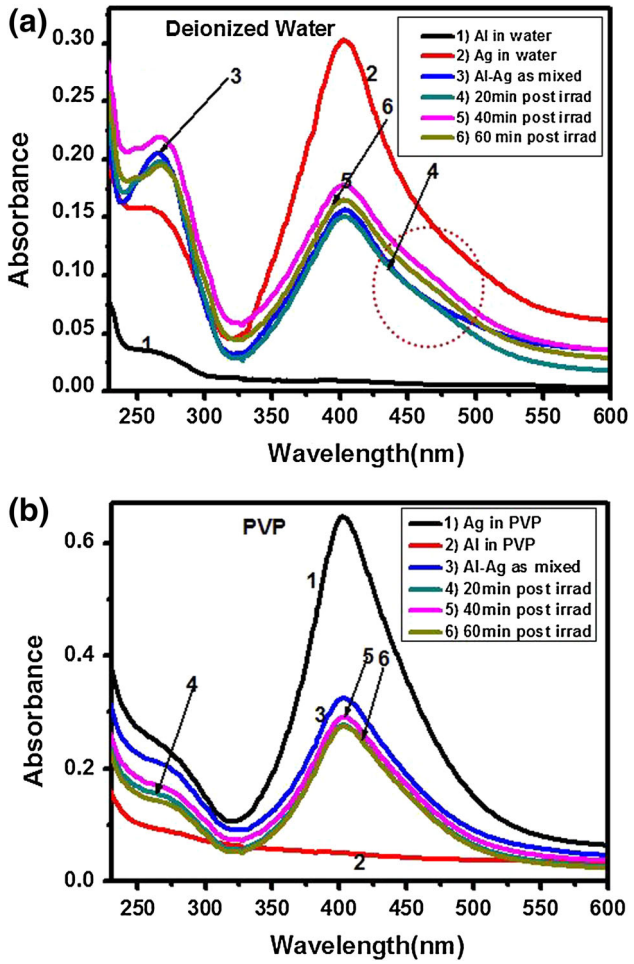

Fig. 6 UV–Vis spectra of Al, Ag, as-mixed Ag–Al and Ag–Al nanocomposites post-irradiated for different times in **a** deionized water and **b** 0.001 mM aqueous PVP solution

wavelength from 220 to 264 nm in water with time is ascribed to the formation of thin natural aluminium oxide shell around highly reactive aluminium core. The observed peak at 264 nm is assigned to LSPR peak of Al–Al_2O_3 core–shell structure, and the large red shift of 44 nm is attributed to higher refractive index of oxide shell compared to water [59, 63]. The silver NPs show characteristic intense but broad LSPR absorption maximum at 404 nm in the UV–Vis spectrum (curve 2). The as-mixed solution exhibits two distinct absorption maxima at 404 and 264 nm corresponding to Ag and Al–Al_2O_3 nanoparticles, respectively [63, 64]. There is no measurable shift in both LSPR peak wavelengths in the mixed solution (curve 3).

Post-irradiation of the mixed solution for 20 min modifies the absorption spectrum; the broadening increases, the absorbance from Al–Al_2O_3 increases, and there is a shift of 1–2 nm in peak wavelengths, presumably due to weak interaction between adsorbed silver particles and Al–Al_2O_3 in the sintered structure (curve 4). The peak broadening suggests the formation of composite structure in deionized water and the damping of plasmonic response of silver core in the presence of alumina over its surface [56, 59]. The LSPR peak of Al–Al_2O_3 is red-shifted by 5 nm after 40 min of post-irradiation due to either the formation of composites particle or decrease in electron density of aluminium resulting from electron transfer to silver or electron scattering by interfacial defect states (curve 5) [65]. The increased effective refractive index of the porous alumina shell with thickness, due to enhanced diffusion of aluminium through oxide shell, may also cause red shift of the LSPR wavelength [65]. The absorption spectrum of sample post-irradiated for 60 min shows small blue shift of 2 nm in the LSPR peak of Al–Al_2O_3, suggesting decrease in refractive index around Al core due to formation of hollow or void in between the core and shell (curve 6) [34, 66].

Heating aluminium for a longer duration increases the oxidation rate and enhances diffusion of both oxygen and aluminium ion at the interface, which leads to increase in oxide shell thickness and red shift of the LSPR peak from 264 to 269 nm. Also, longer irradiation induces hollowing effect (Kirkendall effect) which consequently lowers the effective refractive index and blue-shifted the peak absorption wavelength. Further increase in post-irradiation time does not alter the extinction spectrum. The anisotropy is also evident in UV–visible spectra where large broadening in the spectra around 430–500 nm could be seen (curves 4, 5 and 6). Once the Al_2O_3 starts to nucleate on an Ag, the free electrons from the Ag must compensate for the charge induced by the polarized plane at the interface. As the Ag particle has only a very limited source of electrons, this compensation makes all other facets of the Ag NP electron deficient and unsuitable for multi-nucleation, giving only the dumbbell structure or anisotropic structure.

The UV–visible spectrum of the aluminium NPs in PVP solution shows a featureless spectrum except a high absorbance near 200 nm, as shown in Fig. 6b, curve 1. The LSPR peak of Al–Al_2O_3 at 264 nm, observed in water, is completely missing in the freshly prepared sample and also in sample kept for 4 days. It was found that the aluminium NPs in water agglomerate after 4–5 h of residency time; however, no agglomeration was seen in the PVP solution. Clearly, this demonstrates formation of pure and stable aluminium nanoparticles in PVP solution as well as superior performance of PVP in reducing their oxidation [59, 67, 68]. Also, absorption spectrum reveals the enhanced efficiency of nanoparticle generation in the PVP solution due to strong plasma confinement effect during the laser ablation. The ablation products when emitted from the metal plate like Ag and Al are confined by the solvent; the confinement is stronger for high-density and viscous solvent [69]. The generated plasma already confined near

solids is at high pressure and temperature and therefore can etch the surface and again generate NPs through secondary ablation [69]. Therefore, the increase in the ablation efficiency of the PVP solution is due to the increased density and viscosity of solvent by PVP. The absorption spectra clearly show that PVP not only improves the oxidation stability of the aluminium NPs but also increases the formation efficiency [59]. With increasing post-irradiation time, the peak absorption at 404 nm related to silver NPs reduces along with small blue shift in peak wavelength, and simultaneously, the absorption near 264 nm related to Al–Al_2O_3 increases very slowly in comparison with sample prepared in water (curves 4–6).

4 Conclusion

We have demonstrated the fabrication of nanometre-sized Ag–Al_2O_3 rattle-type nanoparticles by a simple and environmental friendly method based on pulsed laser heating of colloidal nanoparticles in water and polymer solution. The spherical rattle-type particle consists of solid silver core encapsulated by thin porous Al_2O_3 shell with hollow region between core and shell. By controlling time of irradiation, different morphological structures such as sintered structure, core–shell and rattle-type structure were obtained in water and polymer solution. The UV–Vis spectroscopy provided evidence of formation of aluminium oxide and aggregation in water as well as weak oxidation and high stability in the polymer. Further, this approach could also be used for fabrication of rattle particles with tunable core/shell, variable air gap between core and shell and high surface area; such rattle particles are expected to be useful for applications in bio-separation and catalysis because of their porous structure and for molecular detection via shell-isolated surface-enhanced Raman spectroscopy.

Acknowledgments The authors would like to gratefully acknowledge support received from TEM and HRTEM facilities at IIT Delhi.

References

1. Y. Zhao, L. Jiang, topic. Adv. Mater. **21**, 1 (2009)
2. R. Nakamura, D. Tokozakura, H. Nakajima, J. Appl. Phys. **101**, 074303 (2007)
3. J. Chen, R. Zhang, L. Han, B. Tu, D. Zhao, Nano Res. **6**, 871 (2013)
4. B. Guan, T. Wang, S. Zeng, X. Wang, D. An, D. Wang, Y. Cao, D. Ma, Y. Liu, Q. Huo, Nano Res. (2013). doi:10.1007/s12274-013-0392-9
5. Y. Yin, R.M. Rioux, C.K. Erdonmez, S. Hughes, G.A. Somorjai, A.P. Alivisatos, Science **304**, 711 (2004)
6. J. Zhou, C. Tang, B. Cheng, J. Yu, M. Jaroniec, Appl. Mater. Interfaces **4**, 2174 (2012)
7. M.E. Davis, Nature **417**, 813 (2002)
8. V. Valtchev, L. Tosheva, Chem. Rev. **113**, 6734 (2013)
9. X. Fang, Z. Liu, M.-F. Hsieh, M. Chen, P. Liu, C. Chen, N. Zheng, ACS Nano **6**, 4434 (2012)
10. L. Wang, T. Fei, J. Deng, Z. Lou, R. Wang, T. Zhang, J. Mat. Chem. **22**, 18111 (2012)
11. J. Li, X. Liang, J.B. Joo, I. Lee, Y. Yin, F. Zaera, J. Phys. Chem. C **117**, 20043 (2013)
12. Q. Zhang, I. Lee, J.B. Joo, F. Zaera, Y. Yin, Acc. Chem. Res. **46**, 1816 (2013)
13. Y. Yang, J. Liu, X. Li, X. Liu, Q. Yang, Chem. Mater. **23**, 3676 (2011)
14. B. Stephan, M. Fumitaka, J. Phys. Chem. C **115**, 4985 (2011)
15. S. Ikurumi, S. Okada, K. Nakatsuka, T. Kamegawa, K. Mori, H. Yamashita, J. Phys. Chem. C **118**, 575 (2014)
16. J.A. Rodriguez, M. Kuhn, J. Hrbek, J. Phys. Chem. **100**, 18240 (1996)
17. V. Evangelista, B. Acosta, S.S. Miridonov, E. Smolentseva, S. Fuentes, A. Simakov, Appl. Catal. B Environ. **518**, 166–167 (2015)
18. R. Ferrando, J. Jellinek, R.L. Johnston, Chem. Rev. **108**, 846 (2008)
19. N. Toshima, T. Yonezawa, New J. Chem. **22**, 1179 (1998)
20. V. Amendola, M. Meneghetti, Phys. Chem. Chem. Phys. **15**, 3027 (2013)
21. S. Barcikowski, G. Compagnini, Phys. Chem. Chem. Phys. **15**, 3022 (2013)
22. H. Zhang, G. Duan, Y. Li, X. Xu, Z. Dai, W. Cai, Cryst. Growth Des. **12**, 2646 (2012)
23. P. Liu, Y. Liang, X. Lin, C. Wang, G. Yang, ACS Nano **5**, 4748 (2011)
24. K.Y. Niu, J. Yang, S.A. Kulinich, J. Sun, H. Li, X.W. Du, J. Am. Chem. Soc. **132**, 9814 (2010)
25. S.-H. Tsai, Y.-H. Liu, P.-L. Wu, C.-S. Yeh, J. Mater. Chem. **13**, 978 (2003)
26. R. Singh, R.K. Soni, J. Nanosci. Lett. **3**, 11 (2013)
27. H.J. Fan, M. Knez, R. Scholz, D. Hesse, K. Nielsch, M. Zacharias, U. Gosele, Nano Lett. **7**, 993 (2007)
28. M. Zhen, D. Sheng, ACS Catal. **1**, 805 (2011)
29. H.M. Chen, R.S. Liu, J. Phys. Chem. C **115**, 3513 (2011)
30. S. Lee, J.H. Shin, M.Y. Choi, J. Nanopart. Res. **15**, 1473 (2013)
31. L. Samain, A. Jaworski, M. Edén, D.M. Ladd, D.-K. Seo, F.J. Garcia-Garcia, U. Haussermann, J. Solid State Chem. **217**, 1 (2014)
32. S.A. Al-Mamun, R. Nakajima, T. Ishigaki, J. Colloid Interface Sci. **392**, 172 (2013)
33. G. Bajaj, R.K. Soni, J. Nanopart. Res. **12**, 2597 (2010)
34. L. Zhang, D.A. Blom, H. Wang, Chem. Mater. **23**, 4587 (2011)
35. Y. Li, X.-Y. Yang, J. Rooke, G.V. Tendeloo, B.-L. Su, J. Colloid Interface Sci. **348**, 303 (2010)
36. D.-Y. Liu, S.-Y. Ding, H.-X. Lin, B.-J. Liu, Z.-Z. Ye, F.-R. Fan, B. Ren, Z.-Q. Tian, J. Phys. Chem. C **116**, 4477 (2012)
37. S.Z. Khan, Z. Liu, L. Li, Appl. Phys. A **101**, 781 (2010)
38. J. Wilcoxon, J. Phys. Chem. B **113**, 2647 (2009)
39. T. Salminen, M. Honkanen, T. Niemi, Phys. Chem. Chem. Phys. **15**, 3047 (2013)
40. F.-D. Mai, C.-C. Yu, Y.-C. Liu, K.-H. Yang, M.-Y. Juang, J. Phys. Chem. C **115**, 13660 (2011)
41. Z. Peng, B. Spliethoff, B. Tesche, T. Walther, K. Kleinermanns, J. Phys. Chem. B **110**, 2549 (2006)
42. I. Vladoiu, M. Stafe, C. Negutu, I.M. Popescu, J. Optoelectron. Adv. Mater. **10**, 3177 (2008)
43. R.J. Rothenberg, G. Koren, Appl. Phys. Lett. **44**, 664 (1984)
44. N.J. Hogan, A.S. Urban, C. Ayala-Orozco, A. Pimpinelli, P. Nordlander, N.J. Halas, Nano Lett. 2014. doi:10.1021/nl5016975

45. Z. Fang, Y.-R. Zhen, O. Neumann, A. Polman, F.J.G. de Abajo, P. Nordlander, N.J. Halas, Nano Lett. **13**, 1736 (2013)
46. R. Mahfouz, F.J. Cadete Santos Aires, A. Brenier, E. Ehret, M. Roumie, B. Nsouli, B. Jacquier, J.C. Bertolini, J. Nanopart. Res. **12**, 3123 (2010)
47. L. Zhang, H. Jing, G. Boisvert, J.Z. He, H. Wang, ACS Nano **6**, 3514 (2012)
48. H. Yu, M. Chen, P.M. Rice, S.X. Wang, R.L. White, S. Sun, Nano Lett. **5**, 379 (2005)
49. R. Huang, Y.-H. Wen, Z.-Z. Zhu, S.-G. Sun, J. Phys. Chem. C **116**, 8664 (2012)
50. W.H. Qi, S.T. Lee, J. Phys. Chem. C **114**, 9580 (2010)
51. R. Gaudoin, W.M.C. Foulkes, G. Rajagopal, J. Phys. Condens. Matter **14**, 8787 (2002)
52. I. Vladoiu, M. Stafe, C. Negutu, I.M. Popescu, J. Optoelectron. Adv. Mater. **10**, 3177 (2008)
53. M.A. Trunov, S.M. Umbrajkar, M. Schoenitz, J.T. Mang, E.L. Dreizin, J. Phys. Chem. B **110**, 13094 (2006)
54. V.I. Levitas, M.L. Pantoya, G. Chauhan, I.J. Rivero, Phys. Chem. C **113**, 14088 (2009)
55. J. Lee, J. Lee, T. Tanaka, H. Mori, Nanotechnology **20**, 475706 (2009)
56. M.B. Cortie, A.M. McDonagh, Chem. Rev. **111**, 3713 (2011)
57. R. Huang, Y.-H. Wen, Z.-Z. Zhu, S.-G. Sun, J. Phys. Chem. C **116**, 8664 (2012)
58. T. Tsuji, T. Yahata, M. Yasutomo, K. Igawa, M. Tsuji, Y. Ishikawa, N. Koshizaki, Phys. Chem. Chem. Phys. **15**, 3099 (2013)
59. R. Singh, R.K. Soni, Appl. Phys. A (2014). doi:10.1007/s00339-014-8487-z
60. A. Baladi, R.S. Mamoory, Appl. Surf. Sci. **256**, 7559 (2010)
61. Y. Ekinci, H.H. Solak, J.F. Loffler, J. Appl. Phys. **104**, 083107 (2008)
62. E. Stratakis, M. Barberoglou, C. Fotakis, G. Viau, C. Garcia, G.A. Shafeev, Opt. Express **17**, 12650 (2009)
63. Y. Chen, H. Wu, Z. Li, P. Wang, L. Yang, Y. Fang, Plasmonics **7**, 509 (2012)
64. H. Han, Y. Fanga, Appl. Phys. Lett. **92**, 023116 (2008)
65. A.M. Goodman, Y. Cao, C. Urban, O. Neumann, C. Ayala-Orozco, M.W. Knight, A. Joshi, P. Nordlander, N.J. Halas, ACS Nano **8**, 3222 (2014)
66. N.D. Subramanian, J. Moreno, J.J. Spivey, S.S.R.C. Kumar, J. Phys. Chem. C **115**, 14500 (2011)
67. M.D.D. Thi, T.T.L. Thi, F.-B. Thi, C.D. Mau, Adv. Nat. Sci. Nanosci. Nanotechnol. **2**, 015009 (2011)
68. S.Y. Kim, C.F. Zukoski, Langmuir **27**, 10455 (2011)
69. T. Tsuji, M. Nakanishi, T. Mizuki, S. Ozono, M. Tsuji, Y. Tsuboi, Sci. Adv. Mat. **4**, 391 (2012)